Materials Research. 2025; 28:e20240058
DOI: https://doi.org/10.1590/1980-5373-MR-2024-0058

Active Metal Soldering and Characterization of Soldered Joints in Cu Base Plate to Aluminum-Graphite Composites

L. C. Tsao[a*], Yao-Ching Fang[a], Ming-Wei Wu[b]

[a]*National Pingtung University of Science & Technology, Department of Materials Engineering, 91201, Neipu, Pingtung, Taiwan.*
[b]*National Taipei University of Technology, Department of Materials and Mineral Resources Engineering, 10608, Taipei, Taiwan.*

Received: February 06, 2024; Revised: December 23, 2024; Accepted: January 19, 2025

Heat dissipation materials with high thermal conductivity (TC) can meet the high demand for improving heat dissipation in high-power IGBT modules. The current study focused on soldering Al-graphite composites (Al-Gr) with a copper (Cu) base plate using an active type Sn-Ag-Ti (SAT) solder. Ultrasonic active soldering (UAS) was performed in air at 250 °C for 30 sec. The relative spreadability rates of the direct UAS process versus conventional soldering were + 276.6% for SAT/Cu and +186.1% for SAT/Al-Gr. After direct UAS, a Cu_6Sn_5 layer formed at the active solder/Cu interface and Al dissolved into the active solder zone, thus forming a ternary coarse Al-Ag-Sn solid solution in the active solder region. In addition, submicron particles (e.g., Al-Ag-Sn and Ag_3Sn) adsorbed on the surface of active solder/Gr interface. The calculated Gibbs free energy results indicated that both solute Ti and Ti-Sn compounds could react with C to form TiC compounds, and TiC reacted with Ti-Sn compounds to form the Ti_2SnC phase, which was accelerated with the direct UAS process. The shear strengths were measured to be 31.0 ± 4.1MPa for Cu/SAT/Cu joints, 14.3 ± 3.2 MPa for Al-Gr/SAT/Cu joints, and 12.8 ± 3.8 MPa for Al-Gr/SAT/Al-Gr joints, respectively.

Keywords: *Al-graphite composites, Sn-Ag-Ti alloy, Ultrasonic active soldering, Spreading area test, Ti_2SnC.*

1. Introduction

One important function of advanced electronic packaging should be to remove the heat generated by higher-powered electronic components such as power metal oxide semiconductor field effect transistors (MOSFET) and insulated gate bipolar transistors (IGBTs)[1]. According to previous research, approximately 55% of electronic failures are related to high temperature[2]. Moreover, Black's equation[3] indicates that increases in temperature accelerate the decline in reliability and the failure of electronic materials and devices. Therefore, efficient cooling techniques demand both high thermal conduction materials within the package and efficient heat removal from the device[1]. The temperature increase caused by power loss will not only affect the chip performance but also inevitably cause damage to the chip. In general, the failure occurs because of material mismatches among the metal, ceramic, and semiconductor materials, which result in mechanical stress[4]. For example, Cu (400 W/m-K), Al (216 W/m-K) and its alloys are ideal heat sinks because of their high thermal conductivity (TC) values[5]. However, Cu (17 ppm/K), Al (23 ppm/K) and its alloys also have high coefficients of thermal expansion (CTE). Thus, they require a thermal stress compensating material between the attached Si (2.6 ppm/K), SiC (4.0 ppm/K) and GaN (5.6 ppm/K) chips. To meet this requirement, cost-effective materials must be designed to have high TC (> 450 W/m-K), low CTE, mechanical stability, high mechanical damping, suitable machinability, and low production costs. The development of efficient methods of heat dissipation for electronic parts such as chips, circuit boards, and systems is a significant challenge.

Graphite can play an important role in thermal management due to its excellent TC. However, materials in the graphite family (graphite flakes, graphite fibers, expanded graphite or pyrolytic graphite) are brittle[6]. Therefore, common metal matrix composites (MMCs) utilize a ceramic material (e.g., SiC, Al_2O_3) as reinforcement and a low-density metal (e.g., Al, Ti, Mg) as the host matrix[7]. A new class of advanced MMCs, Al-graphite composites (Al-Gr), are materials with low density, high machinability, high mechanical strength, and high TC with customized CTE for applications that require superior performance and high thermal management. These materials have high TC (up to 750 W/m-K) and low weight, making them effective solutions for problems related to the base plate for power IGBT modules[8]. However, sapphire, Al, graphite, and Al-Gr MMCs substrates are well known to be hard-to-wet or non-wetting with common solders[9].

Direct active soldering is an emerging technique for joining a range of materials by utilizing active elements

*e-mail: tlclung@mail.npust.edu.tw

(such as Ti, Zr, Hf and V) to improve the solderability of a non-wetting material[10-13]. This technology can be applied to IGBT modules for low-cost and efficient packaging.

The direct UAS of a light metal (e.g., Al, Ti) with a high entropy alloy has been established[14]. It has been found that the diffusion of all alloying elements of the $Al_{0.3}CrFe_{1.5}MnNi_{0.5}$ high entropy alloy is sluggish in the joint area. Li et al.[15] successfully accomplished both fast (10 s) and low temperature (240 °C) wetting of Si_3N_4 using Sn9Zn2Al solder. It was concluded that the shear strength of the joint increased with a prolonged ultrasonic time. According to bubble dynamic analysis, the high liquid velocity, high temperature, and high pressure are caused by the fast wetting ability. In the hard-wetting and high thermal interface materials of graphite, ultrasonic waves in active solder can facilitate its spread on a porous graphite surface in air[16]. In addition, Wojdat et al.[17] have reported the application of plasma sprayed Cu intermediate layers in the flame soldering process of Al-Gr to 6060-Al alloy. The samples were heated by propane–oxygen flame up to 200 °C, which is the melting temperature of Al flux and Sn40Pb solder. Song et al.[18] achieved success in the metallization layer of graphite using Sn0.3Ag0.7Cu-9 wt.% Cr in vacuum at 950 °C for 30 min. Then the metallized graphite was soldered to copper with Pb-free Sn0.3Ag0.7Cu solder paste at 250 °C for 30 sec in air, and the average shear strength was 25.0 MPa. A previous work has demonstrated the bonding of 6061-Al/Al-Gr using a Pb-free Sn-Ag-Ti-Cu alloy at 250 °C in air. Al from the Al-Gr substrate was dissolved in the active solder and formed the Al-Ag-Sn phase at the interface[19]. Mendoza-Duarte et al. reported that the reactivity of the graphite surface in the aluminum matrix leads to the formation of Al_4C_3 within a few seconds at 250 °C. The Al_4C_3 interphase adversely affects the composite due to its low TC[20]. Few studies have been focused on the UAS of Cu substrate with an Al-Gr base plate in a short time.

The aim of the current work was to study a novel method of direct UAS of Al-Gr MMC and Cu base plate joints with Sn3.5Ag4Ti (SAT) active solder at low temperature in air within a short time. Direct UAS soldering was performed with a fluxless process at a low temperature of 250 °C for 30 sec in air. The spreading area test, microstructure, shear strength and fracture of the joint were investigated.

2. Experimental Procedures

2.1. Materials

In this experiment, the raw materials consisted of Al-Gr, pure Cu (99.99 wt.%) and SAT active solder. The properties of the materials are listed in Table 1. The Al-Gr was prepared by the squeeze casting method. The microstructure is shown in Figure 1. The Al-Gr consisted of the brighter 6061 Al alloy (Al) matrix, gray flakes of graphite (G_f), and black particles of graphite (G_p). The interface between the Al and Gr in Al-Gr contained no voids. In addition, the SAT active solder was used as a filler metal. Details of the synthesis of the Al-Gr alloy and SAT active solder have been presented in a previous work[19].

2.2. Spreading area test

A schematic drawing of the spreading area test is presented in Figure 2. The SAT active solder rods (diameter, 2 mm × length 2 mm, weight about 0.04g) were cut from an SAT active solder wire. The substrate size (e.g., Cu and Al-Gr) was 8.2 mm × 8.2 mm × 1.5 mm, and the slightly rough surface was polished with SiC paper to 1000 grade. Both the bead and substrate were cleaned with acetone in an

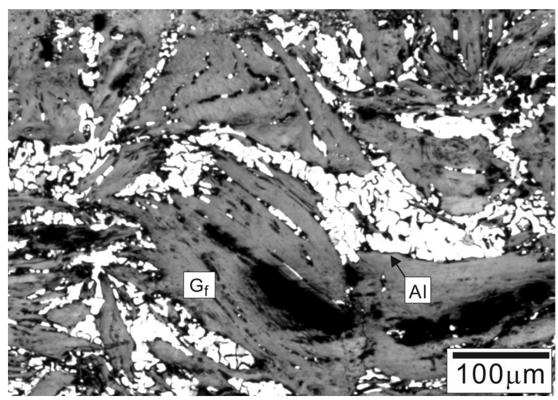

Figure 1. OM micrographs of Al-Gr alloy.

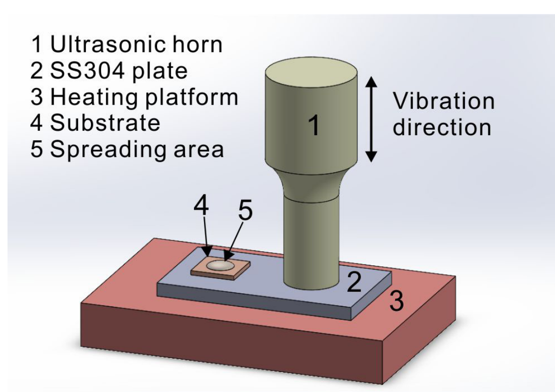

Figure 2. Schematic drawing of the spreading area test.

Table 1. Selected properties of raw material and active solder materials.

Material	Composition
6061-Al	Composition (wt.%) : Mg : 1.07, Si : 0.62, Cu : 0.32, Mn : 0.52, Ti :0.02, Al : balance
Natural graphite	G_f, thickness 735 ± 78.2μm and G_p, diameter 810 ± 45.2μm
Pure Cu	99.99 wt.%
SAT Active solder	Composition (wt.%): Ag : 3.42, Ti :3.95, Mixing rare earth :0.5 Sn : 97.45, Sn : balance

ultrasonic bath. In the spreadability testing, the solder rod was placed on the center of the substrate, conducted out on a hot plate with proportional integral derivative (PID) control at 280 °C for 5 sec in air in the fluxless condition, and allowed to solidify at room temperature. The conventional soldering and UAS process were conducted without (0 sec) and with ultrasonic activation (5 sec), respectively. The spreading area of the active solder was measured by Image J software. Five samples were tested for one parameter and averaged.

2.3. UAS process

The dimensions of the Al-Gr substrate were 10 × 10 × 2 mm^3, and an active solder thickness of 300 μm was ensured by diamond cutting. The substrate was mechanically polished with SiC paper to 1000 grade. Then the polished substrate was ultrasonically cleaned in acetone for 3 min. The soldering was performed on an electric hotplate with thermostatic control in air. Prior to the joining, the Cu sheet (Cu) and Al-Gr were preheated to 250 °C using the hotplate system. The hotplate system was calibrated until the temperature was steady. The temperature of the bond surfaces was measured with a *K*-type thermocouple.

The SAT active solder was set on the bond surfaces of the Cu and Al-Gr. Afterward, the molten active solder was stirred for 30 sec by ultrasonic activation so that the liquid active solder would wet on the sample surfaces. After that, the joints were held firmly in place and cooled in air. To observe the morphology of the interfacial microstructure, the polished cross-sections of Al-Gr/Cu active soldered joints were examined with a metallurgical microscope (Zeiss Axio Scope. A1, Germany) and a Hitachi scanning electron microscope (SEM, Model: S-3000H, Japan; acceleration voltage: 20 kV) equipped with an energy dispersive X-ray spectrometer (EDS).

2.4. Shear testing

The active soldered samples were loaded on a shear strength testing machine (Pin Tai Tech. Co. Ltd., Taiwan) with a constant displacement rate of 0.5 mm/min. Five samples were tested to calculate the average shear strength. The effective joint area was about 10 × 10 mm^2. The morphology of the fracture surface was observed by SEM/EDS.

3. Results and Discussion

3.1. Microstructure of solder material

The microstructure of the SAT active solder is shown in Figure 3. The EDS analysis is provided in Table 2. According to the Ti-Sn phase diagram[21], the microstructure of the SAT active solder (Figure 3) consisted primarily of a β-Sn matrix (Point 1), a grayish-white Ti_2Sn_3 phase (Point 2), black α-Ti (Point 3), a coarse gray Ti_6Sn_5 phase (Point 4), and fine white dispersed Ag_3Sn (Point 5). The composition of the gray phase was 45.18 at.% Ti, 1.01 at.% Ag and 53.81 at.% Sn, corresponding to the Ti_6Sn_5 phase. The solidus and liquidus temperatures of the SAT active solder were determined by DSC curve to be 228.21 °C and 232.54 °C, respectively.

3.2. Spreadability testing

The results of the spreadability testing of the SAT solders are shown in Figure 4 and Table 3. The spreadability testing samples in Figure 4a and 4c were non-wetting in the conventional soldering (without ultrasonic activation). It is clear from Figure 4a that the location of SAT/Cu joining showed slight joining (Point a). However, the strength was lower and the reflowed beads fall out in the ultrasonic cleaning process (Point b). In non-protective atmosphere without flux, the surface of the Cu substrate easily oxidized to Cu oxide at low temperature. Lee et al.[22] reported that the oxidation of copper takes place at low temperature (< 200 °C) within a short duration. As shown in Figure 4b, the addition of ultrasonic activation (5 sec) changed the wetting mode from non-wetting to wetting (Point c) during the direct UAS process, and the surface of the reflowed active solder appeared as a bright mound. In the SAT/Al-Gr, the conventional soldering was non-wetting (Point d, e), as shown in Figure 4c. In the direct UAS process condition, it is clear from Figure 4d that the spreadability of SAT/Al-Gr (Point f) was similar to that of

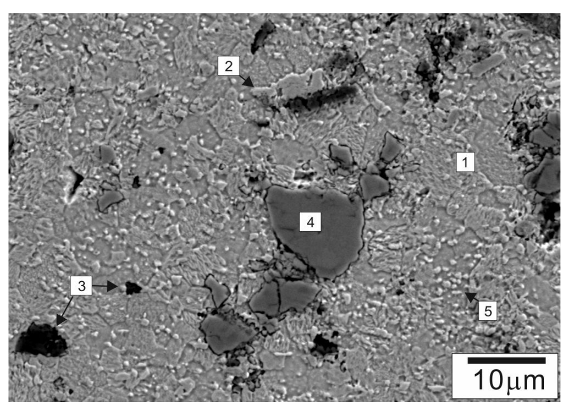

Figure 3. The microstructure of the SAT active solder.

Table 2. Average chemical compositions at different locations (in at.%) on the SAT active solder.

Site	Average chemical composition (at.%)			Phase
	Sn	Ag	Ti	
1	98.47	0.41	0.12	Sn matrix
2	58.57	1.12	40.31	Ti_2Sn_3
3	1.58	-	98.42	α-Ti
4	45.18	1.01	53.81	Ti_6Sn_5
5	27.56	72.44	-	Ag_3Sn

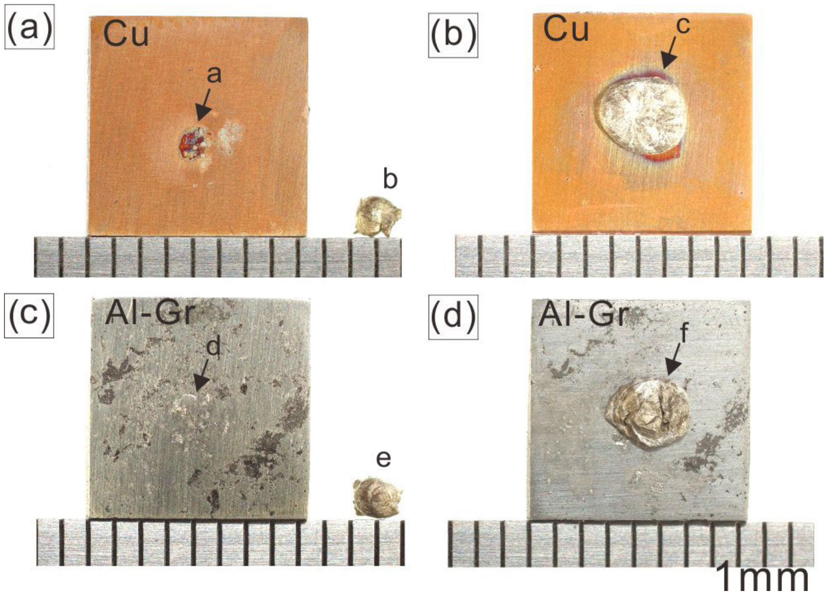

Figure 4. Spreadability testing of SAT solders: (a, b) for Cu substrate, (c, d) for Al-Gr, (a, c) conventional soldering and direct UAS process.

Table 3. Spreadability of SAT active solder on substrate.

Substrate	Soldering method	Wetting condition	Spreading area (mm^2)	The relative variable ratio of direct UAS against conventional soldering.
Cu	Conventional	Non-wetting	2.87 ± 0.31	-
	UAS	Full wetting	10.81 ± 0.55	+ 276.6%
Al-Gr	Conventional	Non-wetting	3.31 ± 0.38	-
	UAS	Full wetting	9.47 ± 0.67	+ 186.1%

SAT/Cu. However, the surface of the SAT/Al-Gr solder ball exhibited dark gray wrinkles. The spreading areas of SAT/Cu were 2.87 ± 0.31 mm^2 for conventional soldering and 10.81 ± 0.55 mm^2 for the direct UAS process. In addition, the spreading areas of SAT/Al-Gr were 3.31 ± 0.38 mm^2 for conventional soldering and 9.47 ± 0.67 mm^2 for the direct UAS process. The relative spreadability rates of direct UAS soldering versus conventional soldering were +276.6% for SAT/Cu and +186.1% for SAT/Al-Gr. These results confirmed that ultrasonic activation obviously improved the spreadability.

3.3. Joint analysis

The direct active soldered joint was fabricated at 250 °C for 30 sec. Figure 5 presents SEM micrographs of the Cu/SAT/Cu solder joint, and EDS analyses were conducted to identify the phase structures and compositions of the IMCs. The EDS results of the corresponding positions of the active solder area are provided in Table 4. It can be seen that the active solder joints consisted of three areas: (i) the solder zone, (ii) an IMC layer and (iii) the Cu substrate. As shown in Figure 5a, the microstructure of the active solder joint consisted of α-Sn matrix, black α-Ti (Point A1), dark gray Ti_6Sn_5 (Point A2), and gray Ti_2Sn_3 (Point A3) in the active solder area. According to the EDS results (Table 4), the atomic percentages of Sn, Cu and Ti in the scallop-shaped IMC layer (Point A4) were respectively 53.18 at.%, 46.61 at.% and 0.31 at.%, indicating that the IMC layer was composed of the Cu_6Sn_5 phase[23]. In addition, the Cu_3Sn phase was not observed at the active solder/Cu substrate interface (Figures 5b and 5c).

Since SAT alloy is a near-eutectic Sn3.5Ag alloy, a tiny change in composition is required for the liquid solder at the liquid–solid interface to become supersaturated and for Cu_6Sn_5 IMCs to form rapidly[24].

In the SAT-Cu system, Cu diffuses into liquid SAT solder to form the Cu_6Sn_5 phase, which nucleates heterogeneously at the liquid/Cu interface and grows continually until a successive thin layer of Cu_6Sn_5 is formed at the interface[25]. However, these Ti-based phase particles (e.g., α-Ti (1670 °C), Ti_6Sn_5(1490 °C) and Ti_2Sn_3 (750 °C)) have high melting or peritectic temperatures[21]. Furthermore, the high temperature Ti_2Sn_3 phase undergoes the peritectic reaction at 750 °C ($Ti_2Sn_3 \leftrightarrow Ti_6Sn_5 + L$). During UAS processing, first, the liquid solder resulted in dissolution of Ti from the surface of the Ti-based phase. Then this dissolution reaction of Ti into liquid solder continued until the solder became supersaturated. Finally, with further cooling, the eutectic reaction of $L \rightarrow Sn + Ti_2Sn_3$ occurred in the Ti-Sn system at 231.9 °C. Therefore, the Ti_2Sn_3 phases developed during the solidification process.

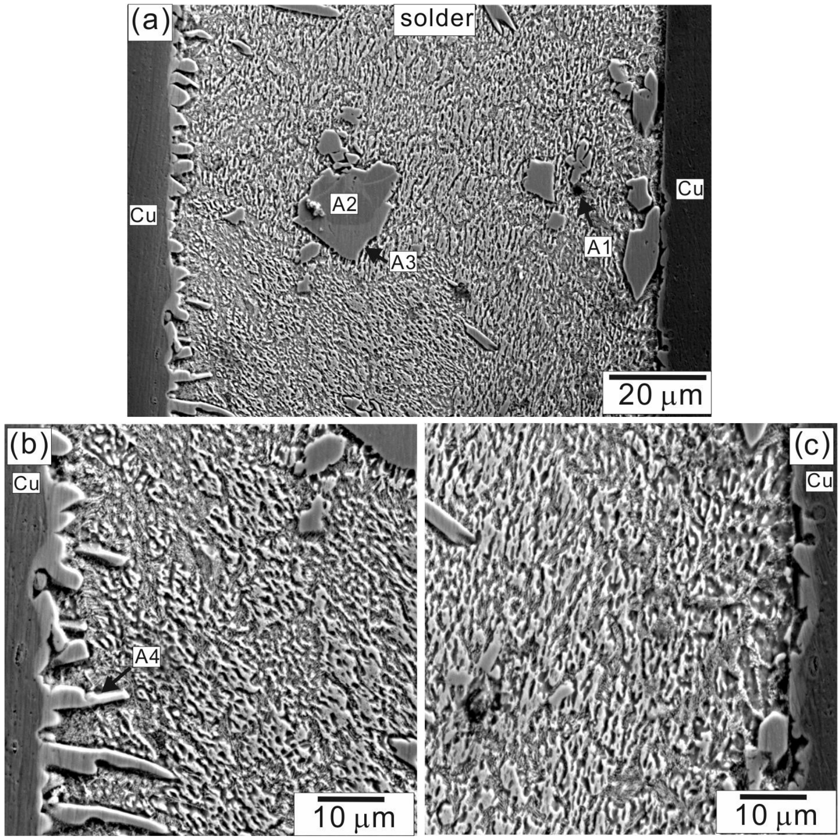

Figure 5. Microstructures at the interface after active soldering: (a) Cu/Cu; (b) Higher magnification (left); (c) Higher magnification (right).

Table 4. EDS results taken from different locations (in at.%) as denoted in Figures 5-7.

Site	Sn	Ag	Ti	Cu	Al	C	Component
A1	0.85	0.56	98.59	-	-	-	α-Ti
A2	48.80	0.64	48.87	1.69	-	-	Ti_6Sn_5
A3	57.99	0.32	40.80	0.89	-	-	Ti_2Sn_3
A4	53.18	-	0.31	46.51	-	-	Cu_6Sn_5
B1	4.53	0.43	81.66	-	2.07	11.31	Ti-Sn-C (α-Ti+TiC_{1-x}+Ti-Sn+Ti_2SnC)
B2	48.75	46.13	0.42	-	4.70	-	$(Ag, Al)_3Sn$
B3	3.11	82.28	0.36	-	14.25	-	Al-Ag-Sn
C1	65.20	34.24	0.56	-	-	-	α-Sn +Ag_3Sn
C2	56.59	0.56	0.89	39.4	2.56	-	α-Sn +Cu_6Sn_5

In general, Al, Gr and Al-Gr show excellent non-wetting properties[26]. Figure 6 presents SEM micrographs of the Al-Gr/SAT/Al-Gr soldered joint. In the high-resolution images of the Al-Gr/SAT solder zone (right side, Figure 6b) and SAT solder zone/Al-Gr (left side, Figure 6c), it can be clearly observed that the joint interfaces had no cracks or voids, indicating close contact between the active solder and Al-Gr. The Al base element of the Al-Gr substrate was clearly dissolved by the melted solder, as shown in Figure 6a, and many IMC grains were observed in the α-Sn matrix of the solidified active soldered area.

On the active solder/Al-Gr side, an elementary mixture of Ti-Sn-C compounds (Point B1) was found. The formation mechanism of the Ti-Sn-C will be discussed in greater detail below. In addition, it can be seen from Figure 6b that the active solder zone consisted of light gray $(Ag, Al)_3Sn$ (Point B2) in the surrounding Ti_6Sn_5 phase (grayish black) and coarse gray Al-Ag-Sn (Point B3). In addition, it was found that small particles of Al-Ag-Sn phase and white sub-Ag_3Sn adsorbed on the surface of the Gr interfaces in this study[19]. Previous studies reported that no reaction happened between Al and Sn. However, dissolution of the Al sheet into the

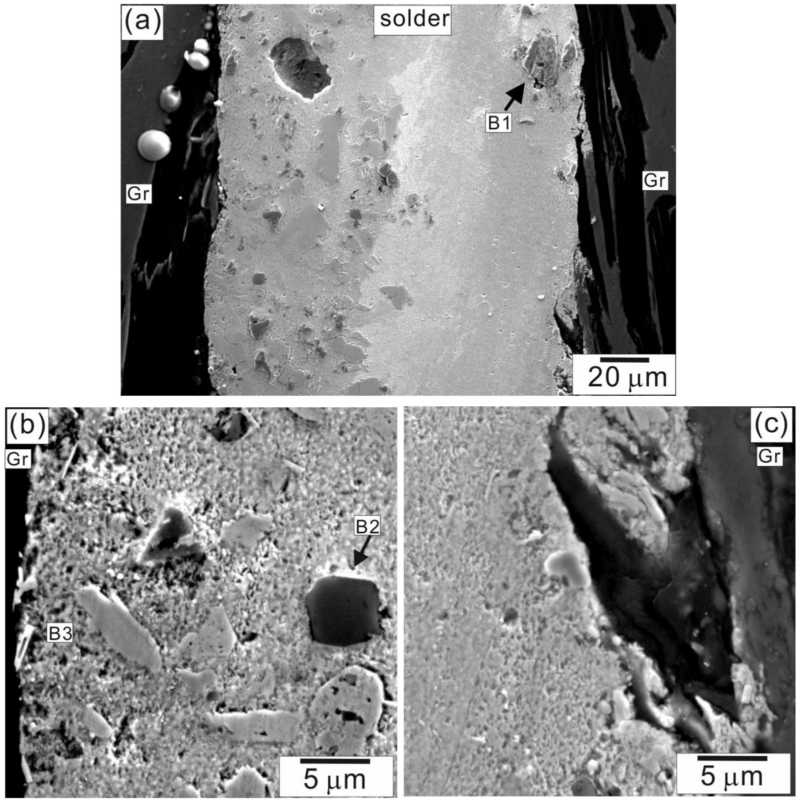

Figure 6. Microstructures at interface after active soldering: (a) Al-Gr/Al-Gr; (b) (a) Al-Gr/soldered zone (left); (c) (a) soldered zone/Al-Gr higher magnification (right).

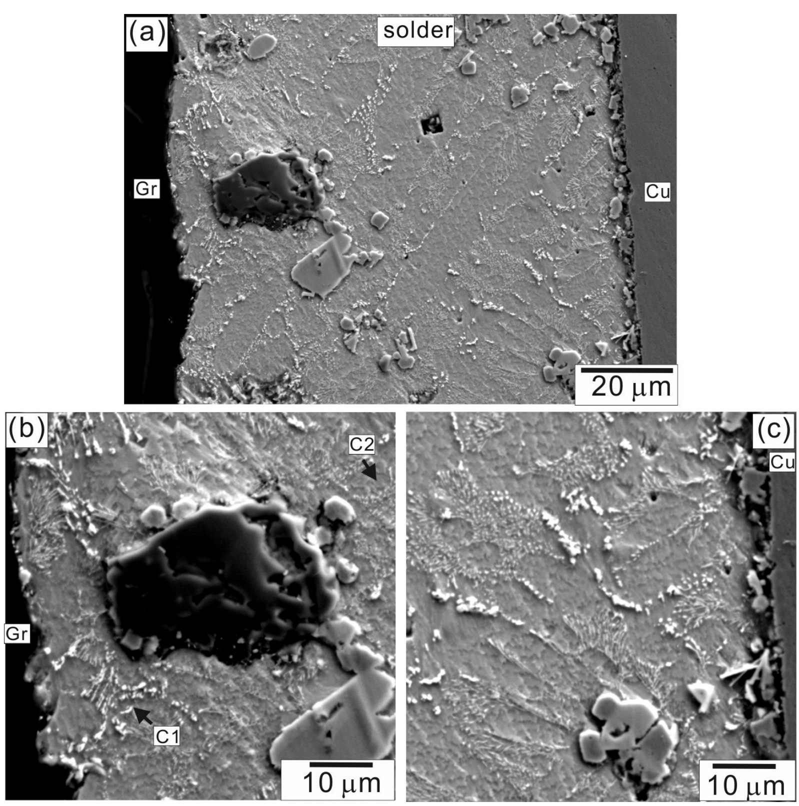

Figure 7. Microstructure of Al-Gr /Gr soldered joints: (a) Al-Gr/Cu; (b) (a) Higher magnification (left); (c) (a) Higher magnification (right).

melted solder during soldering was observed. Al-Ag-Sn solid solution formed at the interface of Sn based solder/Al joints[27]. Li et al. reported that almost all of the diffused Al was exhausted at the interface in the Sn3.5Ag solder joints, with Ag forming a Ag_2Al IMC layer[28].

According to the Al-Sn binary phase diagram[29], the system is a simple eutectic system with limited solid solubilities in the two terminal solid solutions, FCC α-Al and tetragonal β-Sn. First, the solubility of Al in Sn at the eutectic temperature of 228 °C is about 0.6 wt.%. However, the solubility of Al in Sn is very low (near zero) at room temperature[30-32]. Second, the atomic radius of Al (0.143 nm) is similar to that of Ag (0.144 nm), which forms a kind of substitutional solid solution and causes an appreciable replacement phenomenon. Third, the eutectic reaction occurs in the solidification process (L = Sn + Ag_3Sn), Al atoms replace Ag, and Al-Ag-Sn or $(Ag, Al)_3Sn$ IMCs form[30,32].

Figure 7 shows SEM micrographs of a cross-section of the Al-Gr/SAT/Cu interaction interface during the direct active soldering process. The interface of the Al-Gr/SAT/Cu soldered joint was well combined and similar to the Al-Gr/SAT/Al-Gr (Figure 6) and Cu/SAT/Cu (Figure 5) joints, lacking any obvious crack defects. As can be seen in Figure 7b, on the Al-Gr side, the area (Point C1) where the concentration of Ag was high corresponded to eutectic α-Sn + Ag_3Sn. A large area of eutectic α-Sn + Cu_6Sn_5 phases (Point C2) and $(Ag, Al)_3Sn$ nanoparticles was clearly visible in the vicinity of the Al-Gr/active solder interface.

Generally, Sn-Ag-Cu alloys usually consist of an α-Sn, α-Sn + Ag_3Sn or α-Sn + Cu_6Sn_5 binary eutectic structure and an α-Sn + Ag_3Sn + Cu_6Sn_5 ternary eutectic structure[33]. The Cu_6Sn_5 layer phases were clearly visible near the active solder/Cu interface (Figure 7c), demonstrating good wetting of the SAT active solder on both the Al-Gr and the Cu substrate. In general, the SAT active solder used in soldering Cu/Al-Gr is based on Sn-Ag or Sn-Ag-Cu eutectic with trace Ti addition (about 3.5 wt.%). During the direct UAS process, an interfacial metallurgical bond forms owing to element diffusion and chemical reaction, and carbon diffuses into the active solder zone. Both solute Ti elements and Ti-Sn compounds can react with C to form TiC compounds in SAT active soldering to join Cu/Al-Gr. The Gibbs free energy of TiC formation is represented as follows[19,34]:

Ti and C elements can react with each other:

$$\alpha - Ti + C_{(s)} \rightarrow TiC \quad (1)$$

In addition, Ti-Sn IMCs react with C, generating TiC + Sn. The reactions are described as follows:

$$Ti_2Sn_3 + 2C_{(s)} \rightarrow 2TiC(s) + 3Sn_{(l)} \quad (2)$$

$$Ti_5Sn_3 + 5C_{(s)} \rightarrow 5TiC_{(s)} + 3Sn_{(l)} \quad (3)$$

$$Ti_6Sn_5 + 6C_{(s)} \rightarrow 6TiC_{(s)} + 5Sn_{(l)} \quad (4)$$

The Gibbs free energy (ΔG^0) equations (Eqs.) (1), (2), (3) and (4) were calculated and the results are listed in Table 5. At 250 °C (523K), the ΔG^0 of Equations (1–4) for the reactions in Table 5 are -177.36 kJ/mol, -327.62 kJ/mol, -777.98 kJ/mol, and -921.03 kJ/mol, respectively. The negative ΔG values mean that these reactions can occur spontaneously at this temperature. It is suggested that the TiC phase forms at the interfacial region because of the actions of chemical reaction and physical adsorption. Comparing the above results, it is apparent that the free energy of formation of TiC is higher than that of Ti-Sn compounds (Table 5 and Figure 8), and that C atoms can bond with Ti solute atoms from Ti-Sn compounds in interfacial reactions to produce TiC phases at the boundary of graphite[35]. In addition, it has been found that TiC plays a significant role in the Ti-Sn-C

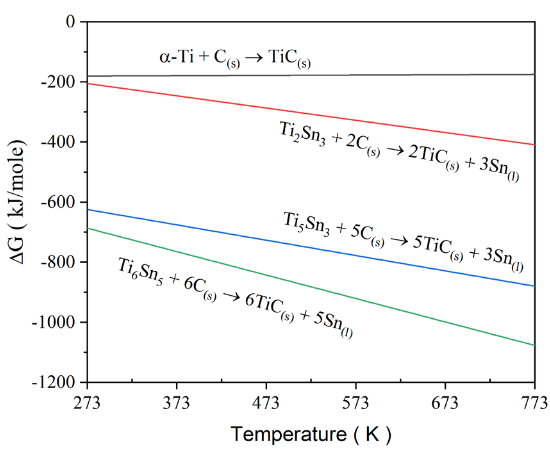

Figure 8. Gibbs free energy (ΔG) of formation of Equations (1-4) as a function of temperature (K).

Table 5. The results of Gibbs energy calculations of the formation of TiC phase at 523 K (250 °C)[30].

	Reaction equations	Gibs free energy (ΔG^o, J/mol)	At 523K (kJ/mol)
1	$\alpha - Ti + C_{(s)} \rightarrow TiC_{(s)}$	- 183,142.62 + 10.0873T	-177.36
2	$Ti_2Sn_3 + 2C_{(s)} \rightarrow 2TiC_{(s)} + 3Sn_{(l)}$	- 94,056.58 - 407.60691T	-327.62
3	$Ti_5Sn_3 + 5C_{(s)} \rightarrow 5TiC_{(s)} + 3Sn_{(l)}$	- 485,459.34 - 510.50988T	-777.98
4	$Ti_6Sn_5 + 6C_{(s)} \rightarrow 6TiC_{(s)} + 5Sn_{(l)}$	- 473,755.85 - 780.58095T	-921.03

system for the formation of Ti_2SnC[36-40]. Furthermore, it has also been found that impurities such as Ti_6Sn_5, Ti_5Sn_3, TiC and Sn accompany Ti_2SnC in these processes[40,41]. Therefore, there is no doubt that TiC reacts with Ti-Sn compounds to form the Ti_2SnC phase. In addition, Yeh et al.[42] have reported the Ti-Sn compound and TiC reaction paths in reactions (5) and (6), represented as follows:

$$Ti_6Sn_5 + 6TiC + Sn \rightarrow 6Ti_2SnC \quad (5)$$

$$Ti_5Sn_3 + 5TiC + 2Sn \rightarrow 5Ti_2SnC \quad (6)$$

Most importantly, the reactions expressed in Equations (5) and (6) may coexist. Therefore, Ti_2SnC can coexist with TiC_{1-x} and Ti_xSn_y[43]. The single intermediate phase (TiC_{1-x}) exists and displays a wide homogeneity range in the Ti-C system[44], ($0.52 < 1\text{-X} < 0.98$). Consequently, this implies that point B1 includes reaction products such as α-Ti, TiC_{1-x}, Ti-Sn and Ti_2SnC phases. In addition, the processes described by Equations (1–6) are accelerated in the direct UAS process.

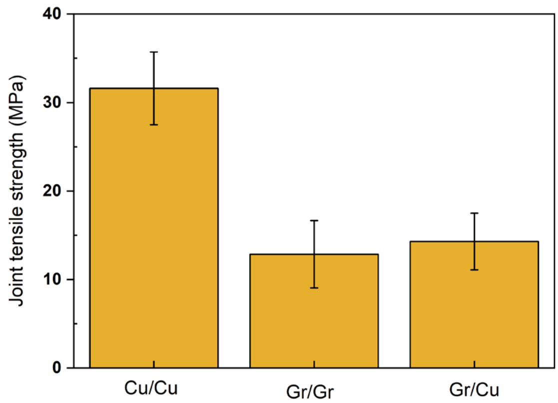

Figure 9. Shear strengths of Cu/Cu, Cu/Al-Gr, and Al-Gr/Al-Gr joints.

3.4. Shear behavior of the solder joints

The joint strengths of the solder joints were investigated with shear tests. Figure 9 displays the average shear strengths of Cu/SAT/Cu, Al-Gr/SAT/Cu and Al-Gr/SAT/Al-Gr joints joined at 250 °C for 30 sec. The order of joint strength at the solder joints was as follows: Cu/SAT/Cu (31.0 ± 4.1 MPa) > Al-Gr/SAT/Cu (14.3 ± 3.2 MPa) > Al-Gr/SAT/Al-Gr (12.8 ± 3.8 MPa). It was found that the microstructure of Cu/SAT/Cu joints had a strong interfacial reaction and interfacial microstructure without any defects. Thus, the joints demonstrated a relatively high shear strength. However, large amounts of $(Ag, Al)_3Sn$ IMCs and Al-Ag-Sn were adjacent to the Al-Gr/active solder interface (Figures 6-7), and the wettability of Al, graphite and Al-Gr is known to be poor[22]. These factors had negative effects on the bonding properties, and thus the shear strengths of Al-Gr/SAT/Cu and Al-Gr/SAT/Al-Gr soldered joints were relatively low.

3.5. Fracture morphology

The fracture morphologies of the Al-Gr/Cu joints active soldered at 250 °C for 30 sec are shown in Figure 10. It was obvious that the active soldered Al-Gr/Cu joints fractured at the interfacial layer between the active solder and Al-Gr. Figures 10a and 10b present the fracture

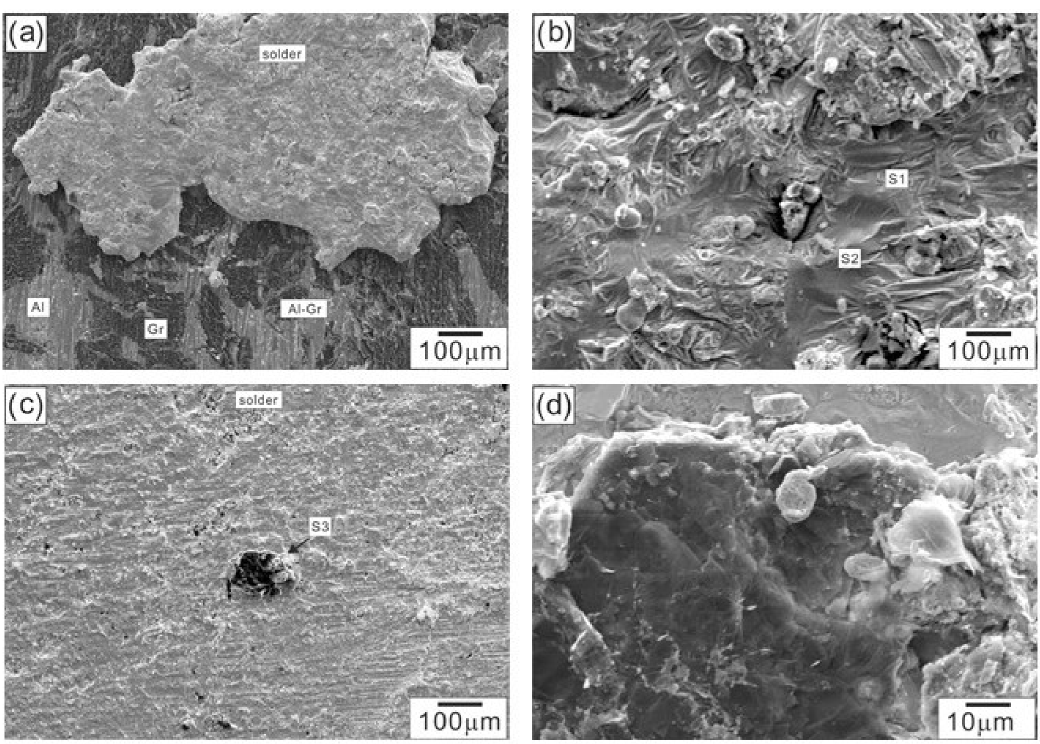

Figure 10. Fractography of Cu/Al-Gr joint bonded with SAT active solder after shear strength testing: (a, b) Al-Gr side; (c, d) Cu side.

morphology of the Al-Gr side. The fractured surface of the Al-Gr substrate remained partially covered with the active solder. The cleavage surface, inter-granular fracture (Point S1) and the second phases (Point S2) can be observed in Figure 10b. The second phases led to both percolating cracks and fracture pores. These second phases may have been the Ti-Sn and Ti-Sn-C phases. In addition, the fractured surfaces on the active solder/Cu joint side are shown in Figures 10c and 10d. The fractured surface remained completely covered with active solder, and some of the bulk-Gr (Point S3) remained in the solder side. These caused stress concentration and crack initiation, which in turn led to a decrease in joint strength.

4. Conclusions

Active soldering of Al-Gr/Cu has been achieved by using a low melting point SAT active solder with a direct UAS process in air at 250 °C for 30 sec. The main conclusions are summarized below:

(1) Ultrasonic activation can obviously improve the spreadability. The relative spreadability rates of direct UAS soldering versus conventional soldering are +276.6% for SAT/Cu and +186.1% for SAT/Al-Gr.

(2) During direct UAS of Cu/Al-Gr joints, (a) a Cu_6Sn_5 layer formed at the active solder/Cu interface; (b) Al dissolved into the active solder zone, thus forming a ternary coarse Al-Ag-Sn solid solution around the active solder layer; and (c) submicron particles (e.g., Ag-Al-Sn, Ag_3Sn) adsorbed on the surface of the Gr interface.

(3) The calculated Gibbs free energy results indicated that both solute Ti elements and Ti-Sn compounds (e.g., Ti_2Sn_3, Ti_5Sn_3 and Ti_6Sn_5) can react with C to form TiC compounds, and TiC reacts with Ti-Sn compounds to form the Ti_2SnC phase, which is accelerated with the direct UAS process.

(4) The shear strengths were measured to be 31.0 ± 4.1 MPa for Cu/SAT/Cu joints, 14.3 ± 3.2 MPa for Al-Gr/SAT/Cu joints, and 12.8 ± 3.8 MPa for Al-Gr/SAT/Al-Gr joints.

(5) The fracture in the Cu/SAT/Al-Gr joints mainly occurred at the active solder/Al-Gr interface.

5. Acknowledgments

The authors acknowledge the financial support of this work by the National Science and Technology Council, Taiwan, under Project No. NSTC 113-2221-E-020-014. SEM was performed by the Precision Instrument Center of National Pingtung University of Science and Technology, Taiwan.

6. References

1. Qian C, Mirza Gheytaghi A, Fan J, Tang H, Sun B, Ye H, et al. Thermal Management on IGBT Power Electronic Devices and Modules. IEEE Access. 2018;6:12868-84.
2. Tong HM, Lai YS, Wong CP. Advanced flip chip packaging. USA: Springer; 2013.
3. Black JR. Electromigration-a brief survey and some recent results. IEEE Trans Electron Dev. 1969;16:338-47.
4. Frear D. Packaging materials. In: Kasap S, Capper P, editors. Handbook of electronic and photonic materials. Cham: Springer International Publishing; 2017.
5. Şevik S, Çiçek B, Özdilli Ö, Aydoğmuş T, Özer Z. Thermal performance analysis of aluminum, copper, and graphene nanoplatelets-doped nanocomposite heat sinks manufactured via stereolithography. Appl Therm Eng. 2023;226:e120315.
6. Ishiharaa M, Sumita J, Shibata T, Iyoku T, Oku T. Principle design and data of graphite components. Nucl Eng Des. 2004;233:251-60.
7. Saxena A, Singh N, Kumar D, Gupta P. Effect of ceramic reinforcement on the properties of metal matrix nanocomposites. Mater Today. 2017;4:5561-70.
8. Yang Y, Dorn-Gomba L, Rodriguez R, Make C, Emadi A. Automotive power module packaging: current status and future trends. IEEE Access. 2020;8:160126.
9. Xu Z, Li Z, Qi Y, Yan J. Soldering porous ceramics through ultrasonic-induced capillary action and cavitation. Ceram Int. 2019;45:9293-6.
10. Tsao LC, Chia YS, Li MC. Joining of SiO2 glass and substrate using In49Sn active solder in air. J Mater Sci: Mater Electron. 2024;35:81.
11. Tsao LC, Li CK, Sun YK, Chang SY, Chuang TH. Fluxless Direct Soldering of Transparent Conductive Oxides (TCOs) to Copper, Advances in Materials Science and Engineering. Adv Mater Sci Eng. 2021;2021:8069719.
12. Koleňák R, Prach M. Research of joining brittle nonmetallic materials with an active solder. Adv Mater Sci Eng. 2014;1:729135.
13. Tsao LC. Microstructural characterization and mechanical properties of microplasma oxidized TiO_2/Ti joints soldered using Sn3.5Ag4Ti(Ce) active solder. J Mater Sci Mater Electron. 2014;25:233-43.
14. Tsao LC, Chan SY, Yu YC. Direct active soldering of Al0.3CrFe1.5MnNi0.5 high entropy alloy to 6061-Al using Sn-Ag-Ti active solder. Trans Nonferrous Met Soc China. 2018;28:748-56.
15. Li Z, Xu Z, Ren B, Yan J. Fast low-temperature ultrasonically soldering porous Si_3N_4 ceramics in the air. Ceram Int. 2022;48:5663-73.
16. Yu W, Liu Y, Liu X. Spreading of Sn-Ag-Ti and Sn-Ag-Ti(-Al) solder droplets on the surface of porous graphite through ultrasonic vibration. Mater Des. 2018;150:9-16.
17. Wojdat T, Sokołowski P, Łatka L, Chmielewska J, Kurantowicz W. Application of plasma sprayed Cu intermediate layers in the soldering process of graphite composite to 6060 aluminum alloy. Mater. 2020;13:5114.
18. Song XG, Chai JH, Hu SP, Cao J, Feng JC, Tang DY. A novel metallization process for soldering graphite to copper at low temperature. J Alloys Compd. 2017;696:1199-204.
19. Tsao LC, Hsieh MJ, Chen TY, Cheng SY, Chen CW. Active soldering of aluminum - graphite composite to aluminum using Sn3.5Ag4Ti0.5Cu active filler. Int J Mater Res. 2016;107:860-6.
20. Mendoza-Duarte JM, Estrada-Guel I, Garcia-Herrera JE, Perez-Bustamante R, Arcos-Gutiérrez H, Martinez-García A, et al. Aluminum carbide formation in Al-graphite composites: in situ study and effects of processing variables and sintering method. Mater Today Commun. 2024;38:108396.
21. Okamoto H. Sn-Ti (Tin-Titanium). J Phase Equilibria Diffus. 2010;31:202-3.
22. Lee SK, Hsu HC, Tuan WH. Oxidation behavior of Copper at a temperature below 300 °C and the methodology for passivation. Mater Res. 2016;19:51-6.
23. Ssunders N, Miodownik AP. The Cu-Sn (copper-tin) system. Bull Alloy Phase Diagr. 1990;11:278-87.
24. Dong C, Shang M, Chen F, Wang Y, Li X, Ma H, et al. Investigation on growth of the orientation-preferred Cu6Sn5 on (001)Cu during the temperature-increased multiple reflow process. J Alloys Compd. 2021;885:161205.

25. Zhao M, Zhang L, Liu ZQ, Xiong MY, Sun L. Structure and properties of Sn-Cu lead-free solders in electronics packaging. Sci Technol Adv Mater. 2019;20:421-44.
26. Xue C, Bai H, Tao P, Wang J, Jiang N, Wang S. Thermal conductivity and mechanical properties of flake graphite/Al composite with a SiC nano-layer on graphite surface. Mater Des. 2016;108:250-8.
27. Yao Y, Zhou J, Xue F, Chen X. Interfacial structure and growth kinetics of intermetallic compounds between Sn-3.5Ag solder and Al substrate during solder process. J Alloys Compd. 2016;682:627-33.
28. Li J, Tatsumi H, Nishikawa H. Comparative Study of Sn-based Solder Wettability on Aluminum Substrate. Quarterly Journal of the Japan Welding Society. 2023;2:26s-30s.
29. McAlister AJ, Kahan DJ. The Al-Sn (Aluminum-Tin) system. Bull Alloy Phase Diagr. 1983;4:410-4.
30. Guo WB, Leng XS, Yan JC, Tan YM. Ultrasonic soldering aluminum at low temperature. Weld J. 2015;94:189s-95s.
31. Tsao LC. Interfacial structure and fracture behavior of 6061 Al and MAO-6061 Al direct active soldered with Sn-Ag-Ti active solder. Mater Des. 2014;56:318-24.
32. Kattner U. Silver-Aluminium-Tin. In: ASM Alloy Phase Diagrams Center. Materials Park, OH, USA: ASM International; 2007.
33. Cui Y, Xian JW, Zois A, Marquardt K, Yasuda H, Gourlay CM. Nucleation and growth of Ag_3Sn in Sn-Ag and Sn-Ag-Cu solder alloys. Acta Mater. 2023;249:118831.
34. Yu WY, Liu SH, Liu XY, Liu MP, Shi WG. Interface reaction in ultrasonic vibration-assisted brazing of aluminum to graphite using Sn-Ag-Ti solder foil. J Mater Process Technol. 2015;221:285-90.
35. Liu SY, Shin YC. Simulation and experimental studies on microstructure evolution of resolidified dendritic TiCx in laser direct deposited Ti-TiC composite. Mater Des. 2018;159:212-23.
36. Yu WY, Liu SH, Liu XY, Liu MP, Shi WG. Interface reaction in ultrasonic vibration-assisted brazing of aluminum to graphite using Sn-Ag-Ti solder foil. J Mater Process Technol. 2015;221:285-90.
37. Lu C, Wang Y, Wang X, Zhang J. Synthesis of Ti_2SnC under Optimized Experimental Parameters of Pressureless Spark Plasma Sintering Assisted by Al Addition. Adv Mater Sci Eng. 2018;2018:9861894.
38. Li SB, Zhai HX, Bei GP, Zhou Y. Synthesis of Ti_2SnC from Ti/Sn/TiC powder mixtures by pressureless sintering technique. Mater Lett. 2006;60:3530-2.
39. Bei GP, Li SB, Zhai HX, Zhou Y. Reaction mechanism for synthesis of Ti_2SnC. Mater Res Bull. 2007;42:1995-8.
40. Sun HY, Kong X, Wei S, Yi ZZ, Wang BS, Liu GY. Effects of different Sn contents on formation of Ti2SnC by self-propagating high-temperature synthesis method in Ti-Sn-C and Ti-Sn-C-TiC systems. Mater Sci Pol. 2014;32:696-701.
41. Li SB, Bei GP, Zhai HX, Zhou Y. Bimodal microstructure and reaction mechanism of ti_2snc synthesized by a high-temperature reaction using Ti/Sn/C and Ti/Sn/TiC powder compacts. J Am Ceram Soc. 2006;89:3617-23.
42. Yeh CL, Kuo CW. Effects of TiC addition on formation of Ti_2SnC by self-propagating combustion of Ti-Sn-C-TiC powder compacts. J Alloys Compd. 2010;502:461-5.
43. Vincent H, Vincent C, Mentzen BF, Pastor S, Bouix J. Chemical interaction between carbon and titanium dissolved in liquid tin: crystal structure and reactivity of Ti_2SnC with Al. Mater Sci Eng A. 1998;256:83-91.
44. Frisk K. A Revised Thermodynamic description of the Ti-C system. Calphad. 2003;27:367-73.